Nanoscale domain wall devices with magnetic tunnel junction read and write

E. Raymenants[1,2,a,*], O. Bultynck[1,2,a], D. Wan[1], T. Devolder[3], K. Garello[1], L. Souriau[1], A. Thiam[1], D. Tsvetanova[1], Y. Canvel[1], D. E. Nikonov[4], I. A. Young[4], M. Heyns[1,2], B. Soree[1,2], I. Asselberghs[1], I. Radu[1], S. Couet[1], V.D. Nguyen[1,*]

---

[1] IMEC, Kapeldreef 75, B-3001 Leuven, Belgium

[2] KU Leuven, Kasteelpark Arenberg 44 - box 2450, B-3001 Leuven

[3] Universite Paris-Saclay, CNRS, Centre de Nanosciences et de Nanotechnologies, 91120, Palaiseau, France

[4] Components Research, Intel Corporation, Hillsboro, OR 97124 USA

[a] These authors contributed equally

[*] Corresponding authors: eline.raymenants@imec.be, van.dai.nguyen@imec.be

6

Fast domain wall (DW) motion in magnetic nanostructures is crucial for future spintronic device
concepts. However, a lack of energy-efficient, scalable and industry-relevant ways to electrically
read and write DWs in nanoscale devices impedes practical applications. Here, we demonstrate
that full electrical control of DW devices can be achieved by incorporating typical high DW velocity
materials (i.e., Pt/Co and synthetic antiferromagnetic (SAF) Pt/Co/Ru/Co) into perpendicular
magnetic tunnel junctions (pMTJs). We first show tunneling magnetoresistance (TMR) readout and
efficient spin transfer torque (STT) writing, comparable to current STT-MRAM technology. Based
on time-resolved measurements, we find faster STT switching dynamics in the SAF-based hybrid
free layer than in conventional dual-MgO free layer while maintaining retention stability. We
demonstrate the full operation of DW devices at nanoscale with MTJs enabling electrical read and
write, and a heavy metal enabling spin orbit torque (SOT)-driven DW motion for information
transmission. Beside implications to technology and applications, we show that these devices can
be used as a tool to explore the physics of DW dynamics at nanoscale. Furthermore, using a SAF-
based DW conduit has the potential to enhance device performance with faster and more reliable
DW motion. This proof-of-concept offers a pathway to the technological development of high-
performance and low-power DW-based devices.

Magnetic domain walls (DW) could form a key ingredient in next generation logic and data storage devices [1, 2] such as racetrack memory [3, 4], spin logic [5, 6, 7, 8] and neuromorphic computing [9, 10, 11]. The discovery of high DW velocity governed by the Dzyaloshinskii-Moriya interaction (DMI) and spin-orbit torque (SOT) [12,13,14,15] in ultrathin magnetic layers on heavy metals, the additional exchange coupling torque (ECT) in synthetic antiferromagnetic (SAF) systems [16] and the angular momentum compensation in ferrimagnets [17], were major breakthroughs in the development of fast, high density, and low-energy devices based on DW motion. To enable these materials for practical application, DWs are required to be efficiently written and read at the nanoscale. However, to date, writing of DWs has mainly been performed through magnetic field-based approaches, and read out through either Hall bar devices or magnetic imaging techniques [5, 8, 9, 12, 13, 17, 14]. These schemes play a crucial role in characterizing material properties, but their applicability

33 to DW devices at nanoscale is limited. Therefore, finding energy-efficient ways to electrically write and read DWs

34 is a necessity for practical applications.

35   In this context, the magnetic tunnel junction (MTJ) can be considered as an excellent candidate. Indeed,

36 current spin-transfer-torque magnetic random-access memory (STT-MRAM) technology has demonstrated that

37 MTJs composed of a CoFeB/MgO-based free layer (FL) [18] offer uniquely high TMR readout and low STT

38 writing current. However, the CoFeB/MgO approach faces significant challenges that relate to low DW speed [

39 19] and poor manufacturability [20,21] for a DW conduit (Suppl. Mater. 2.2.).

40   In this study, we present functional DW devices with MTJs enabling electrical read and write using the

41 hybrid free layer (HFL) design concept [22], allowing us to incorporate two well-known high DW velocity

42 materials, *i.e.*, Pt/Co (PtCo-HFL) [12,15], and Pt/Co/Ru/Co where the thickness of Ru is varied to form a SAF- or

43 synthetic ferromagnet (SFM)-based FL, SAF-HFL and SFM-HFL respectively [16, 23]. The HFL design offers a

44 practical solution for the integration process and etch challenges of DW devices in industrial platforms (Suppl.

45 Mater. 2.2.2) [21]. We validate that single MTJs with a HFL stack offer reliable TMR readout signal and efficient

46 STT writing and could therefore be applied as inputs and outputs of a DW device. By time-resolved conductance

47 measurements in single MTJs, we find that the Pt/Co/Ru/Co-based free layer with antiferromagnetic coupling

48 (SAF-HFL) provides faster STT-driven switching dynamics compared to a dual-MgO reference stack. In fully

49 integrated DW devices, we show that DWs can be locally nucleated by STT at input-MTJs and read out by TMR

50 at output-MTJs while the DWs are directionally transported by SOT between input and output. Therefore, we

51 demonstrate full control of a DW device, which can then be used to access both field- and SOT-driven DW

52 dynamics at the nanoscale. Finally, we show that the HFL device proposal offers the possibility to improve DW

53 device performance by selecting a SAF-based DW conduit.

54

55 **Hybrid free layer MTJ stack design for DW-based devices**

56   In the HFL concept, the first FL (FL1) consists of the conventional CoFeB/MgO-based FL, Fig. 1 **a**. The

57   second FL (FL2), deposited onto a heavy metal (HM), serves as the DW conduit which typically consists of a

58   ferromagnet [12], or a SAF-system [16]. FL2 offers high DW speed originating from interfacial DMI, SOT [12,

59   13, 14, 15] and/or ECT [16]. Note that the spacer material between FL1 and FL2 plays an important role in the

60   stack design. Firstly, it serves to decouple the crystallization of CoFeB (FL1) and FL2 as the fcc (111) crystal

61   structure of Co is incompatible with the bcc (001) crystal structure of CoFeB. Secondly, it enables ferromagnetic
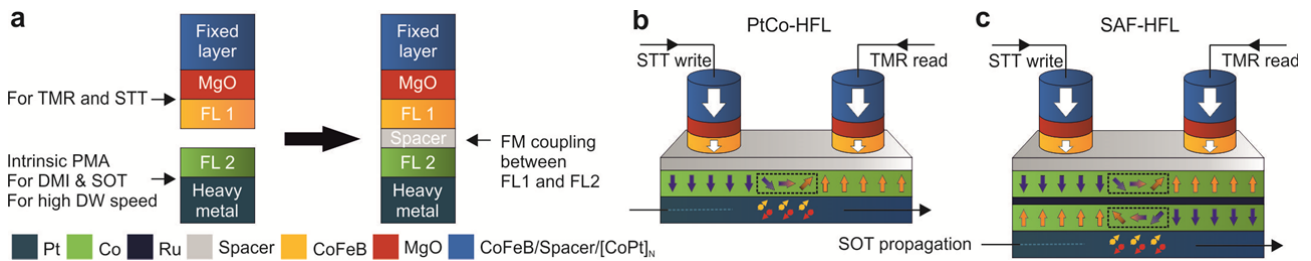

Fig. 1 | Schematic of hybrid free layer concept. (**a**) Hybrid free layer (HFL) concept consisting of FL1(top-left), based on CoFeB/MgO for efficient STT write and high TMR read, and FL2 (bottom-left), consisting of a material with inherent perpendicular magnetic anisotropy (PMA) which is optimized for high DW velocity driven by SOT. The two free layers are ferromagnetically coupled through a spacer layer (right). (**b-c**) Schematic of DW-based devices with PtCo-HFL and SAF-HFL design, respectively. FL2 consists of a Co layer on top of Pt (PtCo-HFL) or of a Co/Ru/Co structure with SFM or SAF coupling, on top of Pt (SFM-HFL or SAF-HFL).

62   coupling between FL1 and FL2 by interlayer exchange coupling, so they behave as a single FL. Additionally, direct

63   growth of an MgO tunneling barrier with bcc (001) crystal structure on Co (FL2) is not trivial due to incompatible

64   crystal structure and poor electron band matching [22]. Therefore, incorporation of the CoFeB layer (FL1) in

65   contact with the MgO barrier is indispensable for retaining high TMR [22, 24] and high STT switching efficiency.

66   In principle, this approach opens the possibility of integrating any high DW speed material in FL2, including

67   ferrimagnets [25], for specific applications such as DW or skyrmion tracks [26,27].

68   Fig. 1 **b-c** illustrate the device concept with Pt/Co and Pt/Co/Ru/Co as DW conduits and MTJs as write

69   and read components. In this proposal, the DW device has three main components in which each one owns its

70   specific functionality: DW writing (*input*), DW transport (*conduit*) and DW reading (*output*). The operation

71   principle is as follows: STT is locally applied at the input pillar to inject DWs into the DW conduit (*i. e.,* DW

72 writing process) via the strong ferromagnetic coupling between CoFeB and FL2 (Extended Data Fig. 1 **a**).

73 Subsequently, the DW travels along the track driven by magnetic field or SOT (Extended Data Fig. 1 **b**) (*i.e.,* DW

74 transport process). The detection of the DW at the output is enabled by TMR (*i.e.,* DW reading process). As a

75 result, this DW device concept simultaneously benefits from efficient STT switching, good TMR owing to the

76 CoFeB/MgO interface, and high DW velocity, resulting from a combination of SOT, DMI and/or ECT in the DW

77 conduit materials on heavy metals.

78

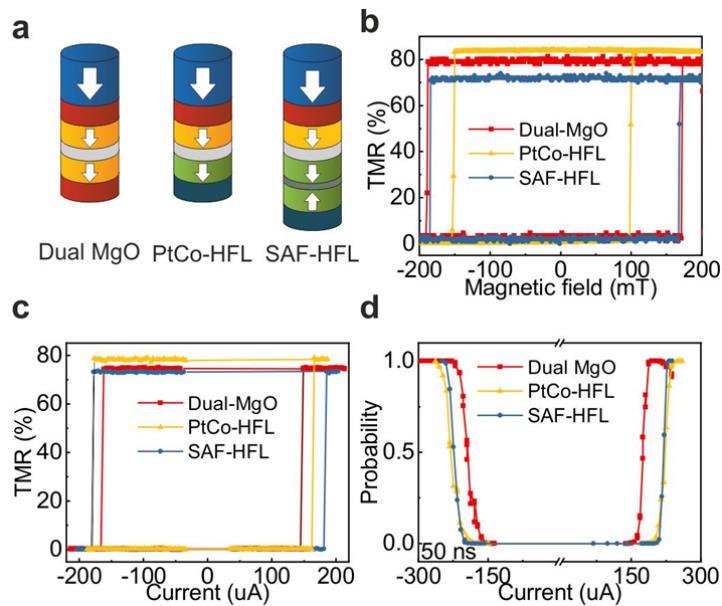79 **Optimized TMR reading and fast STT writing in single MTJ pillar**

Fig. 2 | Hysteresis loops showing reliable TMR and STT in HFL-MTJs. (**a**) Illustration of standard Dual-MgO, PtCo-HFL and SAF-HFL stack, color code similar as in Fig. 1 **a**, (**b**) typical TMR loops as function of perpendicular magnetic field in MTJs with nominal diameter of 60 nm, (**c**) STT induced magnetization reversal at 50 ns pulse width, (**d**) switching probability distribution measurement averaged over 1000 events per point.

80   To verify the applicability of the HFL concept, we studied the magnetic properties of single MTJs made

81   with different types of HFL (Fig. 2 **a**), fabricated on 300 mm wafers using standard processes of MRAM

82   technology. Fig. 2 **b-c** display typical square TMR hysteresis loops of an MTJ pillar as function of field and current

83   pulse, respectively. Importantly, we obtain similar TMR values, about 80 %, and STT switching currents, about 200

84   µA, in all types of FL. This result suggests that the obtained TMR and STT efficiency are mainly contributed by the

85   CoFeB/MgO/CoFeB interfaces as expected in a conventional STT-MRAM device [18, 28]. Note that the lower

86   coercivity in the PtCo- HFL device is linked to our choice of relatively low anisotropy in the stack design (Suppl.

87   Mater. 3.2.1). The switching probability dependence of write current amplitude (Fig. 2 **d**) verifies the deterministic

88   STT switching in all devices (Suppl. Mater. 4.3). A slightly lower write current (~ 170µA) was found in dual-MgO

89   devices, which may be related to the lower damping constant in CoFeB [29] and dual-MgO being an already

90   optimized stack. It is worth to note that the demonstration of good TMR read and reliable STT write in SAF-

91   based FL design opens the path for improving DW transport as SAF systems are expected to be less sensitive to

92   external perturbation and to show fast switching dynamics [23].

93   To evidence this statement, we compare magnetization switching dynamics of the SAF-HFL to a

94   standard dual-MgO based FL using timed-resolved STT-driven switching measurements. The typical time-resolved

95   single shot curves at room temperature, as displayed in Fig. 3 **a**, allow the extraction of three different timescales

96   for every reversal event: the initial incubation delay t_{inc} due to thermal effects, the transition time between stable

97   states t_{trans}, and the pinning time in a pinned state t_{pin}. For a 100 nm device size, it has been shown that the

98   switching process is dominated by a DW-mediated reversal [30]. Note that pinning only occurs in the dual-MgO

99   devices, as reported in Fig. 3 **b**. The varying nature of the pinning level and characteristic pinning timescale

100   indicate that the origin is most likely due to the inhomogeneities of the device microstructure. More specifically,

101   defects in the interfacial MgO/CoFeB anisotropy have been reported to induce pinning in the STT switching

102   process [31].

103   The incubation delays were analyzed under the assumption of a thermally activated process [32]

104    $PDF(t_{inc}) = \exp(-t_{inc}/\tau)/\tau$ where *PDF* is the probability density function. In the thermal limit for small drive

105   currents, where the incubation delay is dominant, we expect the well-known Arrhenius dependence $\tau =$
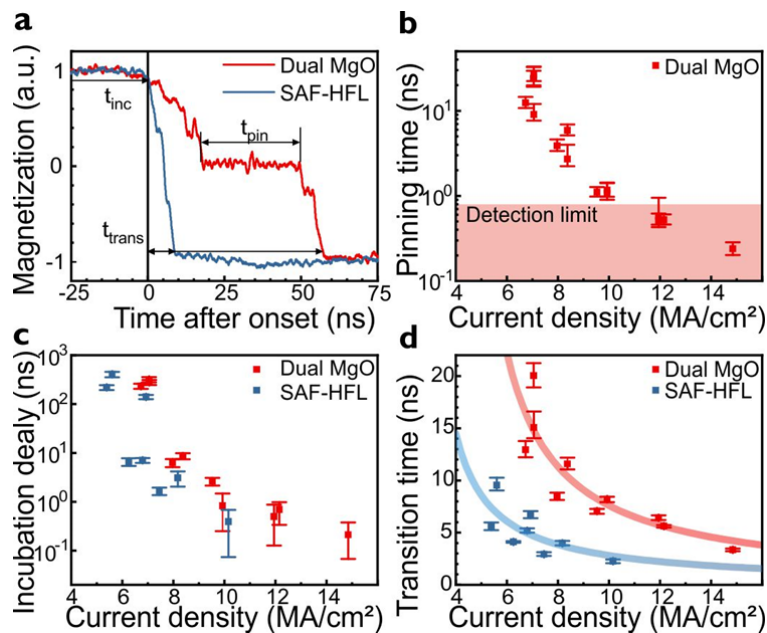

Fig. 3 | Fast STT switching in SAF-HFL without degradation of retention time. (**a**) Typical single-shot curves of the MTJ reversal process lined up to the onset of switching (time 0), defining an incubation delay, transition time, and pinning time. (**b**) Extracted characteristic pinning times, only present in the dual-MgO samples. (**c**) The thermally activated incubation delays as function of current density, demonstrating similar behavior in the two FL designs. (**d**) Transition times vary as function of current density demonstrating consistently faster reversal in the devices with the proposed SAF-HFL. Error bars in all graphs define the 68% confidence interval.

106     $\tau_0 \exp(\Delta[1 - J/J_c])$. However, the absence of analytical expressions for τ_0 in the DW reversal regime will

107   prevent further parameter extraction. As displayed in Fig. 3 **c**, the similar incubation delay as function of applied

108   current indicates similar energy barriers in both stack types (Suppl. Mater. 4.4). It is supposed that in all cases the

109   switching process initiates in the top CoFeB layer (FL1) which is in contact with the STT source from the spin

110   polarization layer. Subsequently, the switching of the whole FL then follows due to the strong coupling with the

111   CoFeB layer. Interestingly, we found that the transition times in the SAF-based devices reduced by a factor of two

112   compared to their dual-MgO counterpart as seen in Fig. 3 **d**. This result suggests that the presence of DMI and

113   antiferromagnetic ECT [16] in our SAF-HFL devices indeed stabilize the DW configuration and lead to shorter

114   transition times.

115

116   **Full electrical operation of DW devices with MTJ write and read**

117   We now demonstrate that a nanoscale DW device with full control can be achieved using the HFL design. In

118   this study, DW devices with MTJs as electrical read and write components have been fabricated consisting of a

119   180 nm wide track shared by three MTJ pillars with a nominal diameter of 80 nm. The pillars are separated by 500

120   nm. We use a Co/Ru/Co FL2 as DW conduit with a 13 Å thick Ru-spacer which allows the formation of a

121   synthetic ferromagnet, SFM-HFL. In such SFM arrangement, the thicker Ru layer ensures PMA of the bottom Co

122   layer even when the interfacial PMA of CFB/MgO is damaged by the etching process. Importantly, the magnetic

123   state of the DW conduit underneath and in between pillars is very similar even if the PMA of the top Co layer has

124   collapsed by the etching process. Therefore, devices with SFM stack design can be used as demonstrators of SOT-

125   driven DW motion where the bottom Co layer is in contact with the SOT source of Pt.

126   TMR versus field loops of three individual pillars connected by a common FL show the coercivity (B_C)

127   overlapping and a significant reduction of switching field (propagation field B_P) when STT was initially applied in

128   one of the pillars (Extended Data Fig. 2). It indicates that the PMA of the DW conduit is fully preserved after

129   device integration [18]. This experiment demonstrates that three basic requirements for a functional DW device

130   are guaranteed, *i.e.,* PMA of the DW conduit is preserved, DWs can be locally written in the track by STT and

131   read out by TMR. In addition, a large difference between B_C $(\sim 61\,mT)$ and B_P $(\sim 33\,mT)$ provides a wide

132   operating window for field-driven DW transport without approaching the nucleation-dominated switching regime.

133   We now prove, Fig. 4, that the full operation of read/write using MTJs and both field and/or SOT-driven DW

134   motion can be achieved in a single DW device. Experimentally, the measurement sequence of a DW device with

135   the track shared by three MTJ pillars is summarized as follows. We firstly saturate the device in the parallel (P)

136   state by a negative external field larger than the coercivity. Consecutively, STT is used to selectively write an

137   antiparallel (AP) domain in the center pillar P2, as seen in Fig. 4 **d-e-f** by an abrupt change of magnetization from P

138   to AP in P2 (blue graph). Finally, the motion of DWs through the track induced by field and/or SOT is detected by

139   TMR in the neighboring pillars. Fig. 4 **a**, **d** shows an example of field-driven DW transport in which the device is

140   operated at a constant field of 27 mT ($<<$ $B_C \sim 61 mT$). In this case, the nucleated domain expands from the

141   center pillar to both outer pillars driven by field and assisted by thermal activation. The result of DW motion

142   along the track is observed by TMR read as a change of magnetic state from P to AP in both P1 and P3,

143   demonstrating the isotropic nature of field-driven transport.

144   We now demonstrate that our DW devices can be operated by applying an in-plane SOT current along the

145   track as shown in Fig. 4 **b**, **c**, **e** and **f**. In contrast to field-driven DW transport, the direction of DW motion is

146   selectively manipulated by the current polarity. As seen in Fig. 4 **b**, **e**, we observe a change of TMR in P3

147   indicating DW motion from P2 to P3 with a positive current. Similarly, Fig. 4 **c**, **f** shows DW motion from P2 to

148   P1 with negative current. Note that we never observe DW motion against the direction of current flow as no

149   switching occurs at P3 (P1) with negative (positive) current (*c.f.*, Fig. 4 **e**, **f**). To verify the device operation

150   reliability, we show in Extended Data Fig. 3 that the experiments are reproducible ~ 100 times.

151   The observation of DW motion along the current flow provides clear evidence that SOT originating from Pt

152   is the main driving force for DW motion in our devices as expected in stand-alone samples [10-13]. In this

153   experiment, the exact shape of the nucleated domain is not obvious since TMR readout is locally sensitive to a

154   change of magnetization state underneath the pillars. However, we believe that a magnetic bubble was fully

155   nucleated under the MTJ as a full switching of MTJ resistance from P to AP is always present after STT write.

156   Also, we do not observe any change of the resistance in the neighbouring pillars during STT write meaning that a

157   domain is locally injected underneath the MTJ. In other words, two DWs are expected to form on each side of

158   the MTJ pillar. It is worth to mention that we do not observe two changes of resistance (*i.e.,* drop of resistance in

159   the input pillar and rise in resistance in output pillar) as would be expected from SOT-driven DW motion (Suppl.

160   Mater. 6.4). It might be due to the fact that the externally applied field favors bidirectional expansion while the

161   SOT-driven DW motion favors unidirectional motion (c.f., Fig. Suppl. 6.4). We believe that fine-tuning of the

162   device integration process will reduce the potential DW pinning sites of the track at nanoscale such that the

163   device can be fully controlled by SOT without external field, as we obtained in the case of stand-alone FL samples

164   (Fig. Suppl. 6.3).

165   Our devices also allow to control DW motion from any pillar in the track. We show in a slightly larger device

166   (track width 200 nm, pillar diameter 100 nm and interpillar spacing 500 nm) that SOT-driven DW motion can be

167   achieved from any pillar where the DW is initially written by STT (Extended Data Fig. 4). This demonstration

168   provides an important feature for practical application of spintronic devices, for instance the operation of spin

169   logic devices which require DWs to be independently controlled from different inputs [6, 8].
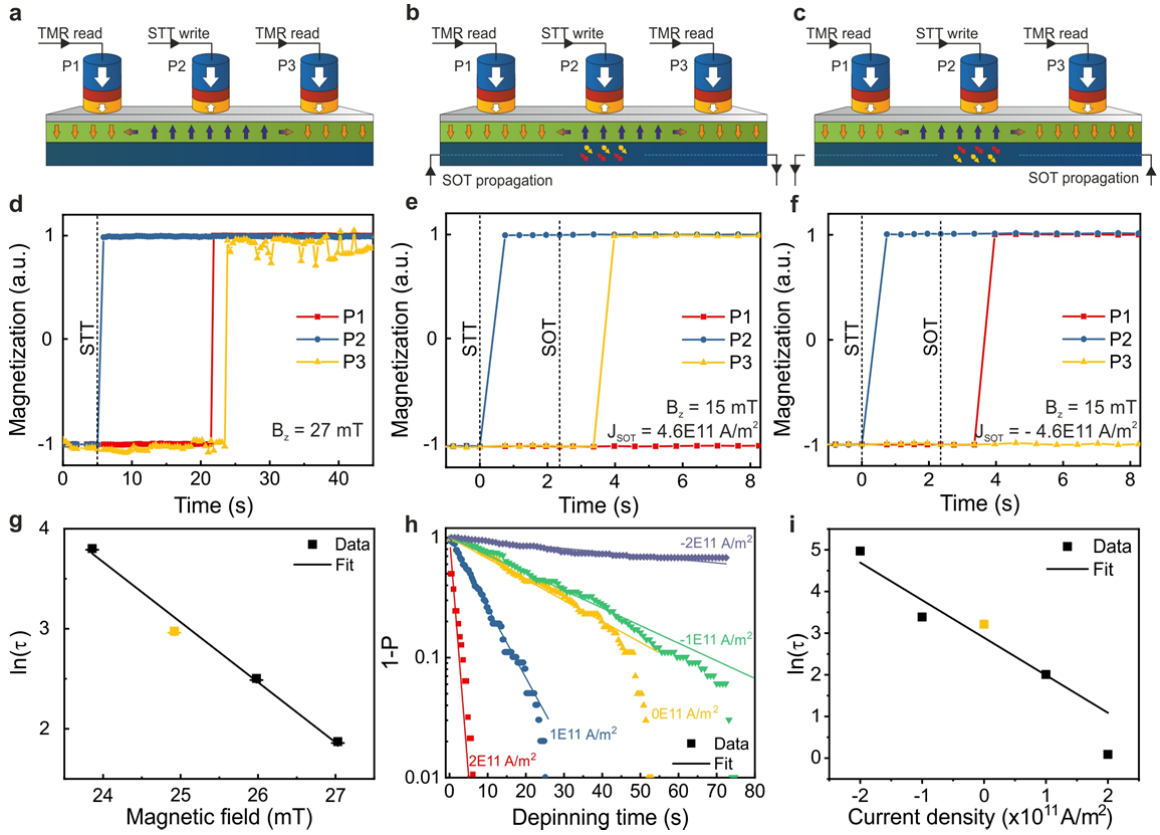
Fig. 4 | Full operation of a DW device with MTJs enabling STT write and TMR readout and SOT-driven DW transport. (**a-c**) Schematics explaining DW transport as observed in (**d-f**) respectively. (**a,d**) Field-driven domain expansion from P2 to both P1 and P3. (**b, e**) SOT-driven DW motion from P2 to P3 with positive current flow in the heavy metal and (**c, f**) SOT-driven transport from P2 to P1 with negative current. (**g**) Natural logarithm of the depinning time as function of external magnetic field. (**h**) Cumulative density functions (plotted as 1-CDF on logarithmic scale) of depinning time at a fixed field of 24.9 mT and varying current density obtained from 100 measurements at each current density and polarity. The data is fitted by an exponential law, resulting in the average depinning times as plotted in (**i**) as function of current.

170   In addition, we prove that such devices offer the possibility to explore DW dynamics in a full operation mode

171   where imaging techniques become ineffective in fully integrated devices at low dimension. For this study, we

172   repeat a similar experiment as seen in Fig. 4 **a** and measure the waiting time for the DW to overcome the energy

173   barrier to travel from P2 (*i.e.,* where DW is written by STT) to P3 (*i.e.,* where DW is detected by TMR read) with

174   the assistance of external field and thermal activation. We choose four different external field values to tune the

175   height of the energy barrier and repeat the measurement 100 times to characterize the statistics of the depinning

176   time at each field value (Fig. Suppl. 6.2.1). The cumulative distribution function (CDF) of depinning time for each

177   field value is well described by a single exponential law, $CDF(t) = 1 - exp(-t/\tau)$ with the characteristic

178   depinning time τ, as theoretically predicted for DW depinning processes [33, 34]. Fig. 4 **g** shows the obtained τ

179   (on ln-scale) as a function of magnetic field, fitted by an Arrhenius-law-based exponential equation $\tau =$

180    $\tau_0 \exp\left(\frac{E}{k_B T}(1 - B/B_{C0})\right)$, where B_{C0} is the intrinsic critical field in the absence of thermal activation [33]. We

181   obtain a thermal stability factor $\frac{E}{k_B T}$ of 38.8 ± 1.

182   Finally, we use such devices as a tool to study the impact of SOT on the DW dynamics in full operation,

183   where the DW is electrically read and written using MTJs. We carry out similar field induced DW depinning

184   measurements and now add SOT on top of a fixed external field of $24.9\ mT$. Fig. 4 **h** displays the CDF of

185   depinning times (on log scale) at varying current density and polarity. As expected, a negative current increases

186   the DW depinning time while a positive current decreases the depinning time (Fig. Suppl. 6.2.2). We find that the

187   CDF of SOT induced DW depinning can also be fitted by a single exponential as expected for DW depinning over

188   a single barrier. It suggests that the application of SOT does not change the nature of DW dynamics in our device.

189   When plotting the obtained depinning time τ (on ln-scale) as function of current density (Fig. 4 **i**), we find that the

190   effect of SOT on the DW depinning dynamics is equivalent with field-driven depinning. Therefore, we assume

191   again an Arrhenius-law based exponential, including the effect of current $\tau = \tau_0 \exp\left(\frac{\Delta}{k_B T}\left[1 - \frac{B}{B_C} - \frac{J}{J_C}\right]\right)$ [34] and

192   approach the effect of current similar to magnetic field. We then obtain $\tau = \tau_0 \exp\left(\frac{\Delta}{k_B T}\left[1 - \frac{B - \epsilon J}{B_C}\right]\right)$ which allows

193   to estimate the SOT efficiency ϵ on the DW depinning process: $\epsilon = 1.5 \pm 0.24\ mT \times (10^{11} Am^{-2})^{-1}$. This is

194   in agreement with literature for PtCo-based stand-alone samples [34], which indicates that the nature of DW

195   dynamics in the conduit layer is retained in nanoscale devices under both field and SOT-driven DW depinning.

196

197

198

199

200   **Toward improvements of DW device performance with SAF-HFL design**

201   The HFL proposal allows to improve device performance, for instance by integration of a SAF system as

202   DW conduit. For this purpose, a softer etching condition in the device integration process was used. Etching was

203   stopped in the reference layer (RL) above the MgO barrier to avoid any magnetic damage to the SAF-based DW

204   conduit, *i.e.,* to the CoFeB/MgO interface of FL1. Note that this etch-stop condition induces an electrical short

205   between the pillars through the RL. We believe that it does not impact the demonstration of field-driven DW

206   motion in this study. We compare the dynamics of field-driven DW motion along PtCo-HFL and SAF-HFL

207   conduits in a 170 nm wide track shared by three MTJs, using real-time TMR detection, Fig. 5 **a** (Suppl. Mater. 6.1).

208   The time resolved single-shot curves in Fig. 5 **b** show a sequential switching of pillars P1, P2 and P3 under the

209   application of the sweeping magnetic field. It suggests that at coercivity, a domain is nucleated and sequentially
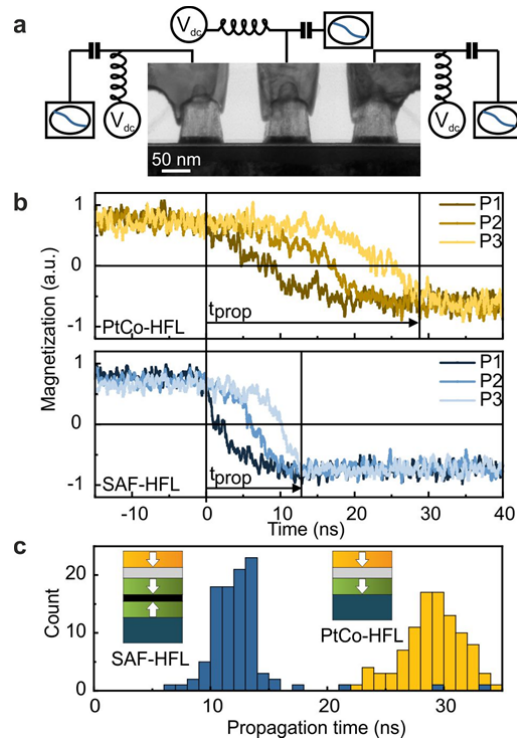

Fig. 5 | Fast DW propagation in SAF-HFL compared to PtCo-HFL. (**a**) Cross-sectional TEM image of 3 MTJs with a nominal diameter of 70 nm and interpillar spacing of 100 nm sharing the same FL. Bias tees enable individual DC and high-frequency access to each pillar. (**b**) Single-shot time-resolved field-driven magnetization reversal at coercivity in PtCo-HFL (42.5 mT) and SAF-HFL (63 mT), (**c**) Propagation time measured from 100 measurements as in **b**, showing shorter propagation time in SAF-HFL.

210   expanded throughout the DW conduit. This measurement reveals that the dynamics of DW motion in high DW

211 speed materials, more specifically in CoPt or in the Co-based SAF system, can be sensed by TMR detection in

212 nanoscale devices. The propagation time, defined as the delay-time between the onset of reversal in P1 and the

213 termination of reversal in P3, is at least double in PtCo-HFL (28.99 ± 2.63 ns) as compared to SAF-HFL (13.09 ±

214 5.48 ns). It means that DW motion in SAF-based devices with an average DW velocity of 42 m/s, is faster than in

215 PtCo-based devices with an average DW velocity of 17 m/s. Faster DW motion in SAF is attributed to the

216 combination of DMI and interlayer exchange coupling which helps to stabilize the DW structure during its motion

217 thus extending the steady motion regime to larger fields compared to its ferromagnetic counterpart. Note that

218 our SAF is not fully compensated (Fig. Suppl. 3.2.2) and that the effect of field on DW motion will be less sensitive

219 if the SAF system is more compensated urging for SOT- rather than field-driven DW motion. Thus, we finally

220 study SOT-driven DW motion in a stand-alone SAF-FL by Kerr microscopy. We indeed observe uniform (Suppl.

221 Video) and fast SOT-driven motion (DW velocity up to *460 m/s* at $J = 3 \times 10^{12}$ *A/m²*) in a SAF-based sample (Fig.

222 Suppl. 6.3). This suggests that a SAF-based DW conduit could enable higher performance DW devices. Therefore,

223 we believe that fine-tuning the MTJ stack design and improving etching conditions to ensure the PMA of the full

224 SAF structure will be key for fast SOT-driven DW motion devices.

225

226 **Conclusions**

227   In summary, we experimentally demonstrated the full operation of a DW device using the HFL-MTJ

228 concept which can provide all requirements for high density and low power DW-based devices including STT

229 write, TMR read and SOT-driven DW motion. This device provides a way to study the physics of DW dynamics

230 under both field and/or SOT at the nanoscale. Moreover, we showed that SAF-based DW conduit devices offer a

231 significant advantage compared to their ferromagnetic counterpart thanks to the characteristic properties of

232 antiferromagnetic materials. These include faster STT writing speed in a single MTJ device and uniform and fast

233 DW motion in the SAF-based DW conduit devices. Therefore, in combination with an optimized manufacturing

234 process of nanoscale devices, we believe that this HFL device concept not only leads the way towards the

235 practical realization of DW-based devices but also shows promise for the development of other potential

236 spintronic devices, such as skyrmion and spin-wave based devices.

1. Dieny, B. *et al.*, Opportunities and challenges for spintronics in the microelectronics industry. *Nature*

Electronics **3** (8), 446-459 (2020).

2. Manchon, A. *et al.*, Current-induced spin-orbit torques in ferromagnetic and antiferromagnetic systems. *Reviews of Modern Physics* **91** (3), 035004 (2019).

3. Parkin, S., Hayashi, M. & Thomas, L., Magnetic domain-wall racetrack memory. *Science* **320** (5873), 190-194 (2008).

4. Blasing, R. *et al.*, Magnetic Racetrack Memory: From Physics to the Cusp of Applications Within a Decade. *Proc. IEEE*, 1-19 (2020).

5. Allwood, D. A. *et al.*, Magnetic domain-wall logic. *Science* **309** (5741), 1688-1692 (2005).

6. Nikonov, D., Bourianoff, G. & Ghani, T., Proposal of a spin torque majority gate. *IEEE Elec. Dev. Lett.* **32** (8), 1128 - 1130 (2011).

7. Hu, X., Timm, A., Brigner, W. H., Incorvia, J. A. C. & Friedman, J. S., SPICE-only model for spin-transfer torque domain wall MTJ logic. *IEEE Trans. Electron Devices* **66** (6), 2817-2821 (2019).

8. Luo, Z. *et al.*, Current-driven magnetic domain-wall logic. *Nature* **579**, 214–218 (2020).

9. Siddiqui, S. *et al.*, Magnetic domain wall based synaptic and activation function generator for neuromorphic accelerators. *Nano Lett.* **20** (2), 1033-1040 (2019).

10. Grollier, J. *et al.*, Neuromorphic Spintronics. *Nat. Electron.*, 1-11 (2020).

11. Yue, K., Liu, Y., Lake, R. K. & Parker, A. C., A brain-plausible neuromorphic on-the-fly learning system implemented with magnetic domain wall analog memristors. *Sci. Adv.* **5** (4), eaau8170 (2019).

12. Miron, M. *et al.*, Fast current-induced domain-wall motion controlled by the Rashba effect. *Nat. Mater.* **10**, 419–423 (2011).

13. Emori, S., Bauer, U., Ahn, S.-M., Martinez, E. & Beach, G. S., Current-driven dynamics of chiral ferromagnetic domain walls. *Nat. Mater.* **12** (7), 611-616 (2013).

14. Avci, C. O. *et al.*, Interface-driven chiral magnetism and current-driven domain walls in insulating magnetic garnets. *Nat. Nanotechnol.* **14** (6), 561-566 (2019).

15. Thiaville, A., Rohart, S., Jue, E., Cros, V. & Fert, A., Dynamics of Dzyaloshinskii domain walls in ultrathin

magnetic films. *EPL* **100** (5), 57002 (2012).

16. Yang, S.-H., Ryu, K.-S. & Parkin, S., Domain-wall velocities of up to 750 m/s driven by exchange-coupling torque in synthetic antiferromagnets. *Nat. Nanotechnol.* **10** , 221–226 (2015).

17. Kim, K.-J. *et al.*, Fast domain wall motion in the vicinity of the angular momentum compensation temperature of ferrimagnets. *Nat. Mater.* **16** (12), 1187--1192 (2017).

18. Ikeda, S. *et al.*, A perpendicular-anisotropy CoFeB--MgO magnetic tunnel junction. *Nat. Mater.* **9**, 721-724 (2010).

19. Burrowes, C. *et al.*, Low depinning fields in Ta-CoFeB-MgO ultrathin films with perpendicular magnetic anisotropy. *App. Phys. Lett.* **103** (18), 182401 (2013).

20. Raymenants, E. e*t al.*, *Scaled spintronic logic device based on domain wall motion in magnetically interconnected tunnel junctions*, presented at IEDM, 2018 (unpublished).

21. Wan, D. *et al.*, Fabrication of magnetic tunnel junctions connected through a continuous free layer to enable spin logic devices. *Jpn. J. Appl. Phys* **57** (45), 04FN01 (2018).

22. Liu, E. *et al.*, Control of interlayer exchange coupling and its impact on spin--torque switching of hybrid free layers with perpendicular magnetic anisotropy. *IEEE Trans. Magn.* **53** (11), 1-5 (2017).

23. Duine, R., Lee, K.-J., Parkin, S. S. & Stiles, M. D., Synthetic antiferromagnetic spintronics. *Nat. Phys.* **14** (3), 217–219 (2018).

24. Perrissin, N. *et al.*, A highly thermally stable sub-20 nm magnetic random-access memory based on perpendicular shape anisotropy. *Nanoscale* **10** (25), 12187 (2018).

25. Avil'es-Felix, L. *et al.*, Single-shot all-optical switching of magnetization in Tb/Co multilayer based electrodes. *Sci. Rep.* **10** (1), 1-8 (2020).

26. Legrand, W. *et al.*, Room-temperature current-induced generation and motion of sub-100 nm skyrmions. *Nat. Mater.* **19** (1), 34-42 (2020).

27. Dohi, T., DuttaGupta, S., Fukami, S. & Ohno, H., Formation and current-induced motion of synthetic antiferromagnetic skyrmion bubbles. *Nat. Commun.* **10** (1), 1-6 (2019).

28. Hirohata, A. *et al.*, Review on Spintronics: Principles and Device Applications. *J. Magn. Magn. Mater.*, 166711 (2020).

29. Devolder, T. *et al.*, Damping of CoxFe80- xB20 ultrathin films with perpendicular magnetic anisotropy. *Appl. Phys. Lett.* **102** (2), 022407 (2013).

30. Bouquin, P., Rao, S., Kar, G. S. & Devolder, T., Size dependence of spin-torque switching in perpendicular magnetic tunnel junctions. *Appl. Phys. Lett.* **113** (22), 222408 (2018).

31. Alzate, J. G. e*t al.*, *2 MB array-level demonstration of STT-MRAM process and performance towards L4 cache applications*, presented at IEDM, 2019 (unpublished).

32. Brown, W. F. J., Thermal fluctuations of a single-domain particle. *Phys. Rev.* **130** (5), 1677 (1963).

33. Fukami, S., Ieda, J. & Ohno, H., Thermal stability of a magnetic domain wall in nanowires. *Phys. Rev. B* **91** (23), 235401 (2015).

34. Haazen, P. *et al.*, Domain wall depinning governed by the spin Hall effect. *Nature Materials* **12** (4), 299-303 (2013).

35. Metaxas, P. a. J. J. a. M. A. *et al.*, reep and flow regimes of magnetic domain-wall motion in ultrathin Pt/Co/Pt films with perpendicular anisotropy. *Phys. Rev. Lett.* **99** (21), 217208 (2007).

238

239 **Methods**

240 **Sample fabrication**: All devices were fabricated in imec's 300 mm pilot line. First, a buried bottom electrode

241 contact (BEC) process was used to define the bottom electrode. Here, single damascene W metallization was

242 applied two times, first to define BEC feedlines and second to define contact plugs. Next, the W contact plugs

243 were capped by an ultra-smooth TaN seed layer prior to MTJ deposition. The stack is deposited using an

244 ultrahigh vacuum (UHV) multitarget magnetron sputtering system at room temperature without breaking vacuum

245 between depositions (EC7800 Canon-Anelva). Pillars were patterned by 193 nm immersion lithography and a

246 subsequent ion-beam-etch (IBE) at normal and grazing angle for single pillar and DW devices. The DW devices

247 required additional 193 nm immersion lithography double patterning to further define the free layer shape. Finally,

248 dual damascene Cu top contacts were fabricated to provide electrical readout at the individual pillars. The dual

249   MgO FL stack, PtCo-HFL stack, SAF-HFL and SFM-HFL stack consist from bottom to top, of

250     $Co_{20}Fe_{60}B_{20}(9)/Mg(6)/Ta(3)/$ $Co_{20}Fe_{60}B_{20}(11)/MgO(10)$,   of $Pt(30)/Co(8)/W(3)/Co_{20}Fe_{60}B_{20}(8)/MgO(10)$,

251     $Pt(30)/Co(8)/Ru(8.5)/Co(6)/W(3)/Co_{20}Fe_{60}B_{20}(8)/MgO(10)$,   and   of

252     $Pt(30)/Co(8)/Ru(13)/Co(6)/W(3)/Co_{20}Fe_{60}B_{20}(8)/MgO(10)$, respectively. Thicknesses in brackets are provided in

253   Angstrom. The magnetic hard layer (HL) consists of a $Co_{17.5}Fe_{52.5}B_{30}$ reference layer (RL) which is

254   ferromagnetically coupled to a SAF that consists of $Co(12)/Ru(8.5)/Co(6)/Pt(8)/[Co(3)/Pt(8)]_6$. More information on

255   the fabrication process can be found in [21].

256   **Electrical setup**: A detailed scheme of the electrical setup of Fig. 3 is provided in Fig. Suppl. 5.1, this setup

257   allows time-resolved measurements of STT-driven magnetization reversal in single pillars. The measurements

258   were performed on high-frequency capable 100 nm pillars. By applying voltage pulses of varying amplitude and

259   short ramp time (~300 ps) we could study the magnetization dynamics down to the nanosecond regime. The

260   magnetic offset field was compensated for by an external magnetic field during the STT-driven reversal. Prior to

261   the recording of the single shot data, two reference traces were recorded for the P and AP state as described in

262   Suppl. Mater. 5. The single shot data travels between the two recorded reference states, which allow the

263   normalization of the single shot data, as shown in Fig. Suppl. 5.2. For each point in Fig. 3, 100 single shots were

264   recorded.

265   The electrical setup for the DW devices in Fig. 4, consists of a source measure unit (SMU) at each pillar, allowing

266   individual STT-writing and TMR readout in each pillar. An additional SMU is connected to the track to allow in-

267   plane current in the heavy metal. To avoid erroneous signals during SOT-driven DW transport, SMUs at the MTJs

268   are kept floating while a current (100 ms) is applied through the track. Consecutively, each pillar is read out.

269   The electrical setup in Fig. 5, consists of radiofrequency and DC paths enabled by bias tees at each pillar. A DC

270   bias is applied at every pillar during magnetization reversal driven by field. At coercivity, the resistance of the pillar

271   suddenly changes leading to a reflection of the applied current. The recorded rf voltages measured by the 25 GHz

272   oscilloscope then equal the reflected rf current multiplied by the 50 Ω termination of the scope channels.

273

278

Author contributions V.D.N. and S.C. conceived the HFL device concept and managed the project. E.R. and

280 V.D.N performed the SOT-driven DW measurements, E.R., O.B., V.D.N and T.D. performed the time-resolved

281 experiments and interpreted the results with help of K.G., S.C., D.W., I.R., I.A, I.Y., D.N., B.S. and M.H.; Device

282 integration was performed by D.W., Y.C., L.S., A.T. and D.T.; The thin films were deposited by S.C.; E.R., O.B.,

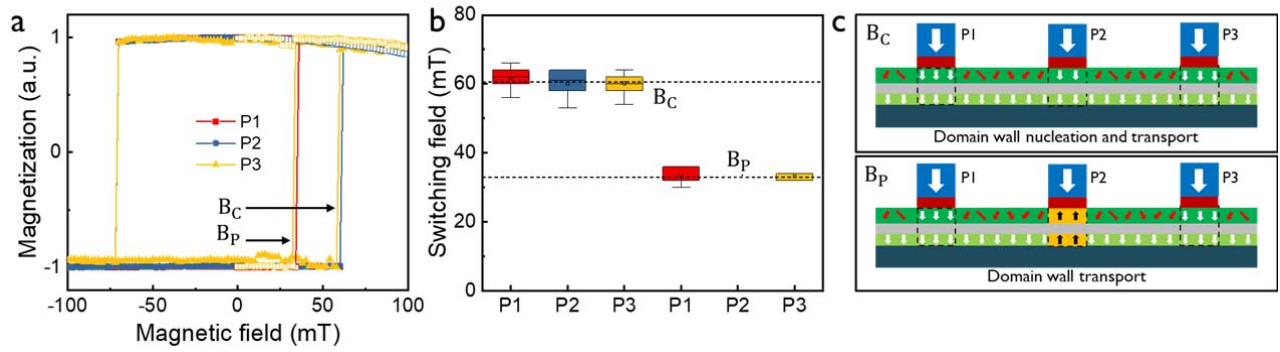283 KG. and V.D.N. wrote the manuscript. All authors discussed the results and commented on the manuscript.

284
285

a

Path for STT write
and TMR read

b

Path for SOT
propagation
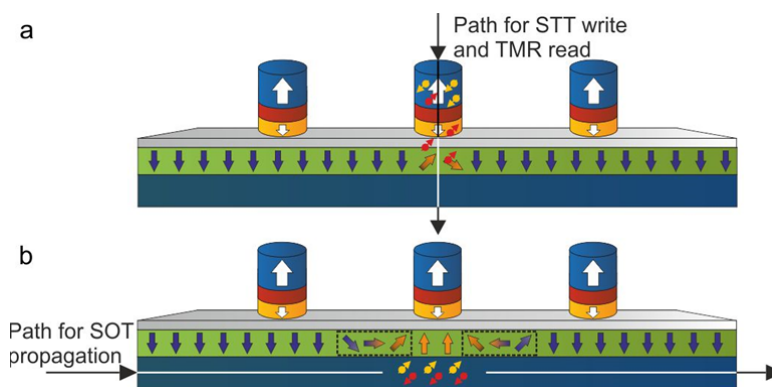
Extended Data Fig. 1 | Representation of current flow. Current path for reading and writing displayed for

center pillar (**a**) and for DW motion driven by SOT (**b**).

287

288

Extended Data Fig. 2 | Comparison of coercive field and propagation field. (**a**) The coercive field B_C is the switching field obtained during a conventional RH loop. The propagation field B_P is obtained after STT-driven nucleation in the center pillar (P2) and consecutive sweeping of the z-field from 0 mT upwards. The domain then expands to the outer pillars (P1 and P3). (**b**) Box plots of the coercive and propagation fields of 10 measurements. The average coercive field is 61 mT while the propagation field to both pillars is only 33 mT. (**c**) Demonstration of the initial state of the device before the RH loops is initiated. Device is fully saturated to obtain coercive field B_C (top), a domain was initially nucleated in P2 to obtain the propagation field B_P (bottom).

289

290
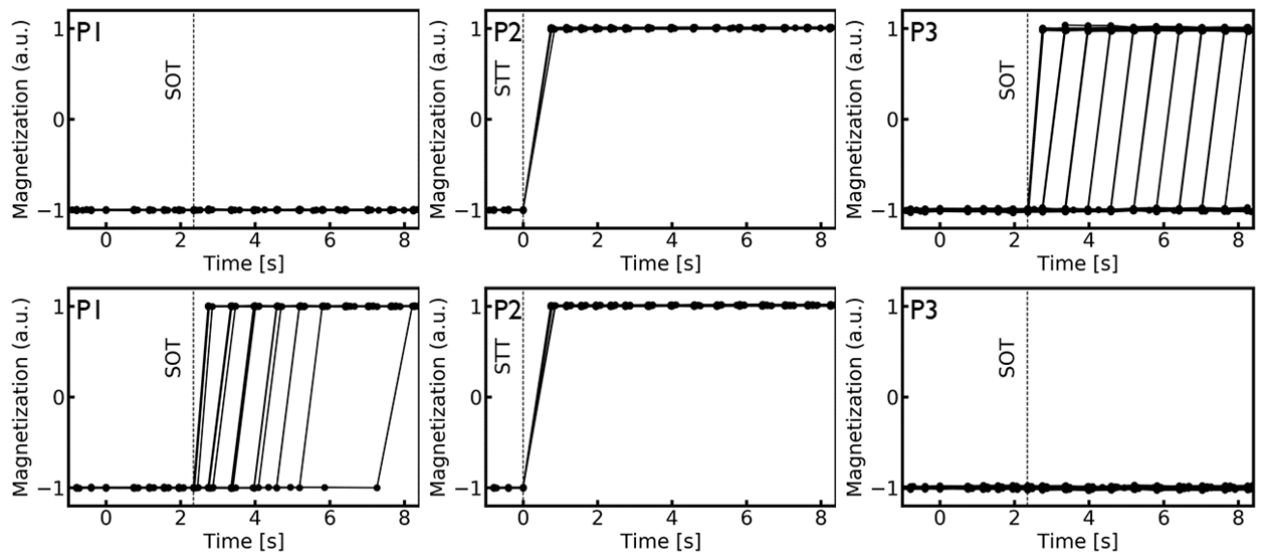
Extended Data Fig. 3 | ~100 x reproducibility of SOT-driven DW transport as in Fig. 4 e, f, STT nucleation in P2 followed by SOT-transport to P3 with positive current (top) and SOT transport to P1 with negative current (bottom). Measurement ~100 x reproducible with each current polarity. The DW never propagates to the reverse direction, i.e. no switch in P1 (top) and P3 (bottom).
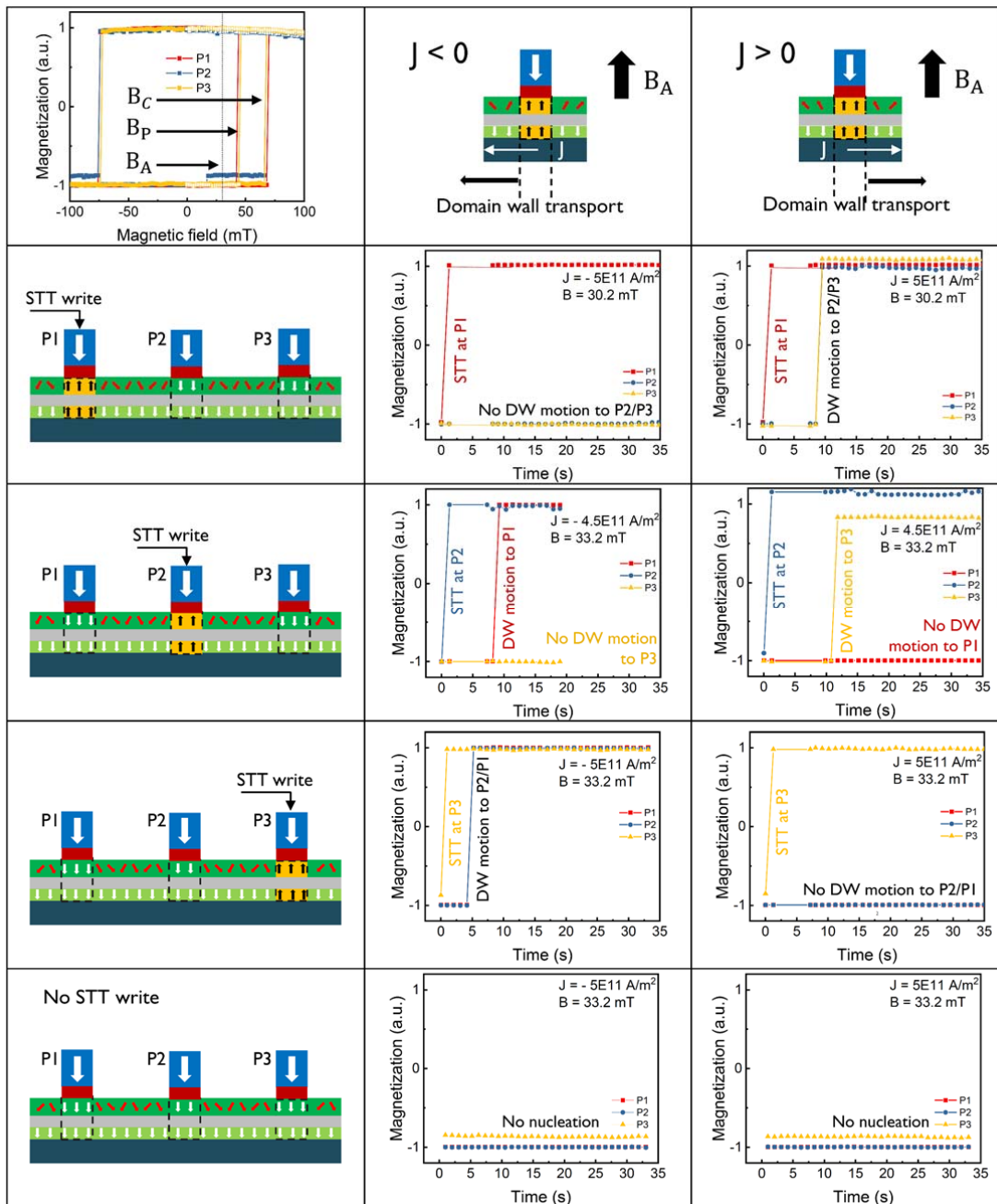
291

292

293

294

295

296

297

298

299

Extended Data Fig. 4 | Full demo of SOT-driven transport starting from each pillar. (Top left) Resistance versus field loop displays the coercive field B_C, the propagation field B_P and the assist field B_A for SOT-driven transport. The schematics at the top display the applied current polarity and direction of DW motion. The domain is nucleated by STT in P1 (second row), P2 (third row), and P3 (fourth row) as shown by the schematics on the left. In the last case (fifth row), no domain is nucleated by STT. The latter confirms that all the above are SOT-driven propagation of DWs, and not SOT-driven switching.
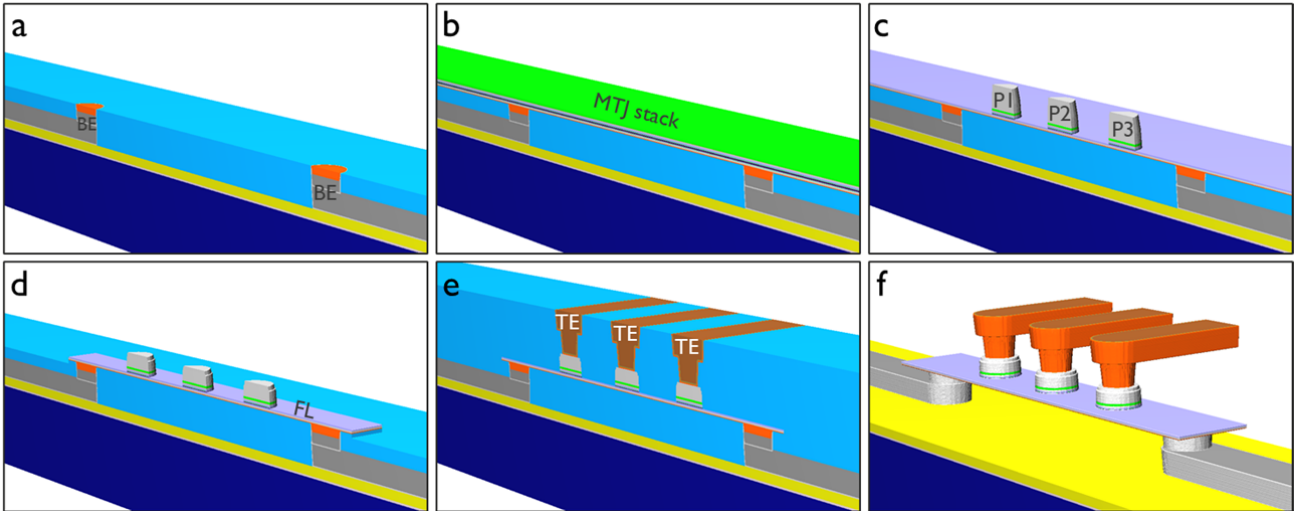
Extended Data Fig. 5 | Fabrication process in imec's 300 mm pilot line. (**a**) Bottom electrode contact (BEC), BEC feedlines and contact plugs were defined. (**b**) MTJ stack deposition using UHV magnetron sputtering system (**c**) Pillar patterning by 193 nm immersion lithography followed by ion-beam-etch (IBE) (**d**) FL shape is defined by 193 nm immersion lithography double patterning (**e**) Dual damascene Cu top contact formation (**f**) 3-dimensional image of DW device with individual TE for each pillar.

301